

Defect Engineering of BCZT-based Piezoelectric Ceramics with High Piezoelectric Properties

Xinjian Wang

University of Jinan

Yu Huan (✉ huanyu19@163.com)

University of Jinan

Yixuan Zhu

University of Jinan

Peng Zhang

University of Jinan

Wenlong Yang

University of Jinan

Peng Li

Liaocheng University

Tao Wei

University of Jinan

Longtu Li

Tsinghua University

Xiaohui Wang

Tsinghua University

Research Article

Keywords: BCZT ceramics, Mn-doping, different sintering atmosphere, p/n-type conduction mechanism, defect engineering

Posted Date: June 14th, 2021

DOI: <https://doi.org/10.21203/rs.3.rs-618581/v1>

License:   This work is licensed under a Creative Commons Attribution 4.0 International License.

[Read Full License](#)

Version of Record: A version of this preprint was published at Journal of Advanced Ceramics on December 24th, 2021. See the published version at <https://doi.org/10.1007/s40145-021-0526-6>.

Defect engineering of BCZT–based piezoelectric ceramics with high piezoelectric properties

Xinjian Wang¹, Yu Huan^{1*}, Yixuan Zhu¹, Peng Zhang¹, Wenlong Yang¹,
Peng Li², Tao Wei¹ & Longtu Li³, Xiaohui Wang³

¹School of Material Science and Engineering, University of Jinan, Jinan 250022, China

²School of Materials Science and Engineering, Liaocheng University, Liaocheng, 252000, China

³State Key Laboratory of New Ceramics and Fine Processing, School of Materials Science and Engineering, Tsinghua University, Beijing 100084, China

Abstract

The intrinsic conduction mechanism and optimal sintering atmosphere of $(\text{Ba}_{0.85}\text{Ca}_{0.15})(\text{Zr}_{0.1}\text{Ti}_{0.9})\text{O}_3$ (BCZT) ceramics was regulated by doping Mn element in this work. By Hall and impedance analysis, the undoped BCZT ceramics exhibit a typical n–type conduction mechanism, and the electron concentration decreases with the increasing oxygen partial pressure. Therefore, the undoped ceramics exhibit best electrical properties ($d_{33} = 585$ pC/N, $k_p = 56\%$) in O_2 . A handful of Mn doping element would transfer the conduction mechanism from n-type into p–type. And the hole concentration reduces with the decreasing oxygen partial pressure for Mn-doped BCZT ceramics. Therefore, the Mn-doped ceramics sintered in N_2 have the highest insulation resistance and best piezoelectric properties ($d_{33} = 505$ pC/N, $k_p = 50\%$). The experimental results demonstrate that the doping Mn element can effectively adjust

*Corresponding authors: Yu Huan: mse_huany@ujn.edu.cn

the intrinsic conduction mechanism and then predicts the optimal atmosphere.

Keywords: BCZT ceramics, Mn-doping, different sintering atmosphere, p/n-type conduction mechanism, defect engineering.

1.Introduction

Lead zirconate titanate based piezoelectric ceramics have been used in many electronic devices, such as sensors, actuators, transducers [1], because of their extraordinary electrical properties and excellent piezoelectric response ($d_{33} \sim 600$ pC/N) [2, 3]. However, lead is toxic, and may cause severe human diseases or environmental problems [4]. Therefore, it is crucial to explore new lead-free piezoelectric systems to replace lead-based piezoelectric materials. In recent years, lead-free piezoelectric ceramics such as BaTiO₃ (BT) [5, 6], (Bi, Na)TiO₃ (BNT) [7, 8], and (K, Na)NbO₃ (KNN) [9, 10] has been extensively studied. Nevertheless, the piezoelectric properties of lead-free piezoelectric ceramics could not compare with the lead zirconate titanate based ceramics.

Therefore, many methods, such as improvement of preparation method [11], optimization of sintering process [12-14], doping strategy, and texturing [15, 16], were applied to construct morphotropic phase boundary (MPB) and polycrystalline phase boundary at room temperature. Excitingly, Ren *et al* modified BT ceramics by introducing Ca²⁺ and Zr⁴⁺ ions to construct the rhombohedral-orthorhombic-tetragonal coexistence at room temperature. And the prepared Ba_{0.85}Ca_{0.15}Zr_{0.1}Ti_{0.9}O₃ (BCZT) ceramics exhibited an ultrahigh piezoelectric constant ($d_{33} \sim 620$ pC/N) [17]. Subsequently, the BCZT-based ceramics attracted tremendous attention and were identified as an ideal candidate for preparing the multilayer piezoelectric devices. To save cost, the base metal (Ni or Cu) should replace the precious metals (Ag, Pt, or Pd)

as internal electrodes [18]. However, the base metal electrode will oxidize under high oxygen partial pressure. Therefore, the BCZT based ceramics should be co-sintered under low oxygen partial pressure with base metal internal electrodes.

There are very few reports on BCZT ceramics sintered under different atmospheres [19-21], and almost none of them illustrate the intrinsic conductivity mechanism. This work adjusted the defect structure of BCZT ceramics by doping Mn elements. The intrinsic conduction mechanism of BCZT ceramics were systematically elucidated by Hall test and impedance spectroscopy. Our study demonstrated that the undoped BCZT ceramics exhibit a n-type conduction mechanism, whereas the Mn-doped BCZT ceramics exhibit a p-type conduction mechanism. Therefore, it is inferred that the optimal sintering atmosphere for undoped and Mn-doped ceramics is O₂ and N₂, respectively. Subsequently, the experimental results verified the prediction.

2.Experimental Procedure

0.25 mol% MnCO₃ doped (Ba_{0.85}Ca_{0.15})(Ti_{0.9}Zr_{0.1})O₃ (BCZT) and pure BCZT powders were prepared using the conventional solid-state reaction method. Barium carbonate (BaCO₃ 99%, Shanghai Macklin Biochemical Co, Ltd.), calcium carbonate (CaCO₃ 99%, Sinopharm Group Co, Ltd.), titanium dioxide (TiO₂ 99%, Tianjin Fuchen Chemical reagents Co, Ltd.), barium zirconium oxide (BaZrO₃ 99%, Alfa Aesar Co, Ltd.), and manganese carbonate (MnCO₃ 99.95%, Shanghai Macklin Biochemical Co, Ltd.) were used as starting materials. The raw materials were

weighed according to nominal stoichiometric composition and then homogenized in a planetary mill for 12 h using ethanol as the milling medium. The obtained slurry was dried thoroughly and then calcined at 1180 °C for 3 h. After that, the mixtures were ball milled for another 12 h. The powders were then compacted into pellets with a diameter of 10 mm and a thickness of 1mm by uniaxial pressing in a stainless-steel die using a polyvinyl butyralas binder. The Mn-doped BCZT specimens were sintered at 1450 °C for 3h in N₂, air, and O₂ with a heating rate of 3 °C/min and a cooling rate of 5 °C/min, which were abbreviated as 0.25Mn-N, 0.25Mn-A, and 0.25Mn-O. And the pure BCZT specimens were sintered at 1500 °C for 3 h in N₂, air, and O₂, which were abbreviated as 0Mn-N, 0Mn-A, and 0Mn-O. For electric measurement, the two main surfaces of the sintered disk samples were coated with silver paste and then heat-treated at 550 °C for 30 min. The disk samples were poled in silicon oil under a direct current electric field of 3 kV/mm at 40 °C for 35 min.

Crystalline structure of the ceramics was determined by X-ray diffraction (XRD; Rigaku 2500, Japan) using Cu K α radiation with a monochromator. High-resolution X-ray photoelectron spectroscopy (XPS) data of the crushed sintered ceramics were obtained using an ESCALab 250 Xi electron spectrometer (Thermo Fisher Scientific, USA). Crystal structure and lattice parameters of samples were analyzed using Rietveld refinements with GSAS software. Raman spectrum in the range from 100 to 1000 cm⁻¹ is measured using 632 nm radiation by a Raman microscope spectrometer (LabRAM HR Evolution, Horiba, France). The quasistatic piezoelectric coefficient d_{33} of the poled ceramics was measured using a quasistatic d_{33} meter (ZJ-3A, Institute

of Acoustics, Chinese Academy of Sciences, Beijing, China). Permittivity ϵ_{33}^T and dielectric loss $\tan \delta$ at 1 kHz were measured using a capacitance meter (Agilent 4294A, Agilent, Santa Clara, USA). The planar electromechanical coupling factor k_p was determined by an impedance analyzer (Agilent 4294A, Agilent, Santa Clara, USA). The temperature-dependent dielectric properties were measured from -50 °C to 200 °C (Agilent 4980A, Agilent, Santa Clara, USA). The ferroelectric polarization hysteresis ($P - E$) loops and electric field - strain ($S - E$) curves were obtained by the TF Analyzer 3000 ferroelectric measuring system (aixACCT Systems GmbH, Aachen, Germany).

3.Results and Discussion

3.1 Phase structure analysis

Figure 1(a) exhibits the XRD patterns of the sintered BCZT ceramics. No secondary phase could be observed in all samples, which indicates that all doping elements (Ca, Zr and Mn) are completely diffused into the BaTiO_3 lattice. In addition, all the samples sintered under different atmospheres have a similar expanded XRD pattern ranging from 44.9° to 45.7° , which demonstrates that the sintering atmosphere has almost no effect on the phase structure. Generally, the diffraction peaks around 45° are indexed as (200) of rhombohedral phase, (022)/(200) of orthorhombic phase or (200)/(002) of tetragonal phase. The multiple peaks around 45° indicate the coexistence of rhombohedral, orthorhombic and tetragonal phases in the BCZT

ceramics. It is also verified by XRD Rietveld refinement in the following section.

Raman spectroscopy is often used to investigate the crystal structure of perovskite ceramics. Figure 1(b) presents the room-temperature Raman spectra of BCZT-based ceramics in the frequency range 100 – 1000 cm^{-1} . Five Raman bands of A (TO_1), A (TO_2), B ($\text{TO}+\text{LO}$), A (TO_3)/E (TO), and A (LO)/E (LO) at 150 cm^{-1} , 208 cm^{-1} , 291 cm^{-1} , 520 cm^{-1} , 720 cm^{-1} , respectively, are observed. The low wave number band is assigned to vibration within the A-site of the perovskite, whereas the high wave number bands could be assigned to vibrations of the TiO_6 octahedra [22]. The main feature of Raman spectra is consistent with tetragonal phase such as the extremely sharp and strong mode at 720 cm^{-1} [23]. The peak mode near 191 cm^{-1} exists in the rhombohedral and orthorhombic phase [24, 25]. The mode around 208 cm^{-1} is the characteristic phonon mode of orthorhombic BaTiO_3 and the peak at 291 cm^{-1} confirms the coexistence of the rhombohedral and tetragonal phase [26, 27]. Therefore, the rhombohedral, tetragonal and orthorhombic phases coexist in the BCZT ceramics. In the Mn-doped BCZT ceramics, the phonon modes of A, B, and E widen, and their peak positions are slightly shifted. It should attribute to the different atomic mass between the doping Mn element and the pristine Ti/Zr elements at the B site. Besides, the Raman intensity of the pure BCZT ceramics is much higher than that of the Mn-doped BCZT ceramics. Considering that the Raman intensity is related to the displacement of B-site cation and the polarizability, the pure BCZT ceramics should exhibit better ferroelectric properties than the Mn-doped BCZT ceramics.

To further discuss the phase structure of ceramics, the temperature dependence of

dielectric constant and dielectric loss at 1 kHz, 10 kHz, 100 kHz, and 1000 kHz are measured in Figures 1(c) and S1. Figure 1(d) summarizes the phase transition temperature of all samples. It can be found that the sintering atmosphere has almost no effect on the phase transition temperature. Combined with the XRD and Raman results, it can prove the coexistence of rhombohedral, orthorhombic and tetragonal phases at room temperature. MPB is constructed at room temperature, which could essentially enhance the piezoelectric performances of BCZT ceramics. Also, the corresponding dielectric loss peak appears at every phase transition temperature. After doping the Mn element, the rhombohedral–orthorhombic transition temperature slightly decreases. Meanwhile, the dielectric loss reduces. The lower dielectric loss is due to the “hardening effect” as the introduction of acceptor Mn element [28, 29].

The element composition and valence distribution of the samples are explored by high-resolution XPS spectra. The binding energy centered at ~777.43 eV, ~346.15 eV, ~457.05 eV, ~178.7 eV correspond to Ba 3d, Ca 2p, Ti 2p, Zr 3d, respectively. Besides, these elements in different samples have nearly the same binding energies, which indicates that the sintering atmosphere has almost no effect on the valence states of the above elements as displayed in Figure S2.

3.2 Defect structure analysis of undoped ceramics

To explore the influence of defect structure on electrical properties, the impedance spectroscopy and Hall measurement are performed on the sample as shown in Figure 2. Figure 2(a) plots the Hall voltage (V_H) as a function of the applied

magnetic field. Hall resistance, carrier type, and concentration are summarized in Table 1 [30]. The results illustrate that the pure BCZT ceramics sintered in all atmospheres exhibit a n-type electron conduction mechanism, which means that the free electron primarily affects the conductivity. The Hall resistance of 0Mn–N, 0Mn–A, and 0Mn–O are $1.54 \times 10^7 \Omega \cdot \text{cm}$, $2.4 \times 10^7 \Omega \cdot \text{cm}$, and $4.38 \times 10^7 \Omega \cdot \text{cm}$, respectively. The carrier concentration (c) could be calculated as follows [31]:

$$c = \frac{1}{(e \times \frac{V_H d}{IB})} \quad (1)$$

Where B , I , e , and d represent the magnetic field, current, electronic charge, and thickness of the bulk ceramic, respectively. The electron concentration of 0Mn–N, 0Mn–A, and 0Mn–O are $4.22 \times 10^7 \text{ cm}^{-3}$, $2.05 \times 10^7 \text{ cm}^{-3}$, and $1.28 \times 10^7 \text{ cm}^{-3}$, respectively. The results indicate that the undoped ceramics sintered at high oxygen partial pressure have higher resistance and lower charge carrier density.

Figure 2(b) shows the impedance spectra of 0Mn–O ceramics measured at 600 °C under pure nitrogen ($PO_2 \sim 10^{-5} \text{ atm}$), air ($PO_2 \sim 0.2 \text{ atm}$), and pure oxygen ($PO_2 \sim 1 \text{ atm}$), respectively. It can be seen from the Nyquist diagram that there are no spikes and arcs associated with Warburg diffusion and oxygen ion conduction. This indicates that the electron carrier is mainly responsible for the conductivity response [32, 33]. The radius of Z^* semicircle increases in the order of N_2 , air, O_2 . It indicates that the resistance of 0Mn–O ceramic gradually increases with the increase of ambient oxygen partial pressure, in accordance with the Hall results.

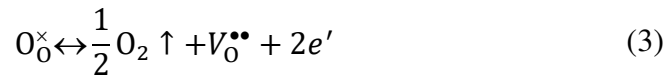
Figures 2(c)–(e) summarize the impedance spectra measured in air at 450–600 °C for the pure BCZT ceramics sintered under different atmospheres. The Nyquist spectra consist of arcs caused by two different electrically active regions, with the left semicircle at high frequency representing a function of grain effect and the right semicircle representing a function of grain boundary effect. To obtain the resistance of grain (R_g) and grain boundary (R_{gb}), the capacitance of grain (CPE1) and grain boundary (CPE2), the Nyquist plots are fitted with the assumed equivalent circuit in the inset of Figure 2(c) on an assistance of Z-view software. The fitting data (red lines) coincides well with the experimental curves. The conductivity (σ_g and σ_{gb}) of grain and grain boundary are calculated by $\sigma = \frac{1}{\rho} = \frac{t}{RS}$ (where σ represents the conductivity of the sample, ρ is the resistivity, t is the thickness of the sample, R is the resistance, and S is the area of the sample). $\ln\sigma$ shows a linearly associated with T^{-1} as displayed in Figure 2(f), demonstrating that the Arrhenius law commonly governs the conductivity. The activation energy (E_a) of the grains and grain boundary could be calculated as follows:

$$\sigma = \sigma_0 \exp\left(\frac{-E_a}{k_B T}\right) \quad (2)$$

Where σ_0 is the high-temperature limit of the conductivity; E_a is the activation energy; k_B is the Boltzmann constant; T is the temperature in Kelvin scale. The calculated E_a values are shown in Figure 2f. The E_a of the grains are 1.1 eV, 1.73 eV, and 1.75 eV, while E_a of grain boundaries are 1.3 eV, 1.83 eV, and 1.98 eV, for 0Mn–N, 0Mn–A, and 0Mn–O samples, respectively. The activation energy expresses the

free energy required for the long-range carrier leap. The lower E_a in the 0Mn–N ceramics declare the free electrons in the ceramics have higher mobility, generating to a significant weakening of the insulating properties.

When the undoped BCZT ceramics are sintered at high temperature, the oxygen ions in the crystal lattice could become oxygen accompanied by the formation of an ionized oxygen vacancy ($V_O^{\bullet\bullet}$) and two electrons (e'), which can be expressed as the following equation.



Therefore, the defects of electrons and oxygen vacancies mainly exist in undoped BCZT ceramics. Since the mobility of the charged oxygen vacancy is significantly weaker than that of the electron, the conduction of the sample should be attributed mainly to the free electron. When the samples are sintered in low oxygen partial pressure, the reaction equation (3) shifts to the right, resulting in a rapid increase of electrons. Therefore, the defect configurations of the pure BCZT ceramics sintered in different atmospheres are sketched in Figures 3a–3c. As the oxygen partial pressure decreases, the number of oxygen vacancies and free electrons gradually increases. Therefore, the pure BCZT ceramics sintered in high oxygen partial pressure tend to have the higher insulation resistivity.

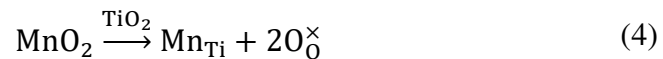
3.3 defect structure analysis of Mn–doped BCZT ceramics

Figure 4 shows the Mn 2p XPS spectra fitted by Gaussian–Lorentz function.

Three fitting peaks from low binding energy to high binding energy correspond to Mn²⁺ (located at 640.5 eV), Mn³⁺ (located at 641.3 eV), and Mn⁴⁺ (located at 642.1 eV), respectively. The content of different Mn elements is shown in Table S1. Compared with other components, the proportion of Mn²⁺ and Mn³⁺ ions in the Mn-doped ceramics sintered in the low oxygen partial pressure decreases, whereas the proportion of Mn⁴⁺ ions increases.

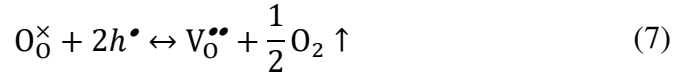
The XRD results are Rietveld refined on an assistance of GSAS software as shown in Figure 5. Table 2 lists all the refined parameters of the BCZT ceramics. And the R_{wp} value is far less than 15%, which shows that the Rietveld refinement results are reliable. The Rietveld refinement confirms the coexistence of rhombohedral, orthorhombic and tetragonal phases in coincidence with the Raman spectra and dielectric constant–temperature curves. And the site occupancies are summarized in Table S2. Additionally, the ion coordination number (CN) and ion radius are shown in Table S3. The Rietveld refinement results demonstrate Mn ions prefer to enter the B site.

Based on the XPS and XRD analysis, the following defect reactions happen in the Mn-doped BCZT ceramics.



The ionic defects of Mn_{Ti} , Mn'_{Ti} , and Mn''_{Ti} primarily exist in the Mn-doped ceramics. In addition, the 0.25Mn-N sample has a high Mn^{4+} content, while the ion defects of Mn^{2+} and Mn^{3+} are dominant in 0.25Mn-O sample. These negatively charged point defects of Mn^{2+} and Mn^{3+} ions could trap positively charged holes, while the equivalent doping Mn^{4+} ions are electrically neutral. The defect configurations of Mn-doped BCZT ceramics sintered in different atmospheres are sketched in Figures 3(d)–(f). When the oxygen partial pressure decreases during sintering process, the concentration of holes in the ceramics decreases.

The defect configuration of the Mn-doped ceramics is also verified by the Hall effect as presented in Table 1 and Figure 6(a). All the Mn-doped ceramics exhibit a p-type conduction mechanism, which means the main charge carrier is hole. The Hall resistance of 0.25Mn-N, 0.25Mn-A, and 0.25Mn-O are $1.28 \times 10^7 \Omega \cdot cm$, $1.04 \times 10^7 \Omega \cdot cm$, and $5.5 \times 10^6 \Omega \cdot cm$, respectively. The carrier concentration of 0.25Mn-N, 0.25Mn-A, and 0.25Mn-O are $1.05 \times 10^8 \text{ cm}^{-3}$, $2.28 \times 10^8 \text{ cm}^{-3}$, and $3.591 \times 10^8 \text{ cm}^{-3}$ respectively. It indicates that 0.25Mn-N has the best insulation performance. Figure 6(b) shows the impedance spectrum of 0.25Mn-N at 600 °C measured in different atmospheres. The semicircle for 0.25Mn-N under nitrogen is larger than that under air and oxygen, which implies that the resistance is highest for 0.25Mn-N. The Hall and impedance measurements confirm that the Mn-doped ceramics exhibit a p-type conduction mechanism. Therefore, equation (7) should exist in the Mn-doped ceramics. When the ceramics are sintered in low oxygen partial pressure, equation (7) shifts towards right, leading to the reducing hole concentration.



Figures 6(c)–(e) summarizes the impedance spectra of ceramics sintered under different atmospheres measured at 450–600 °C in air. The red lines are the fitting results based on an assumed equivalent circuit in inset of figure 6c. As the oxygen partial pressure of the sintering atmosphere decreases, the semicircle measured at the same temperature derived from the grain and grain boundary contribution gradually increases, implying that ceramics sintered in low oxygen partial pressure have a higher resistance. In addition, the E_a of the grains are 1.45 eV, 1.43eV, and 1.12 eV, while E_a of grain boundaries are 1.62 eV, 1.46 eV, and 1.48 eV, for 0.25Mn–N, 0.25Mn–A, and 0.25Mn–O, respectively, as displayed in Figure 6(f). Hence, the holes are more difficult to jump for 0.25Mn–N ceramic because of the higher energy barrier. It implies that the 0.25Mn–N ceramic has better insulating properties.

Therefore, the undoped BCZT ceramics exhibit a n-type conduction mechanism and have the lowest electron concentration in high oxygen partial pressure. The Mn–doped ceramics show a p–type conduction mechanism and have the lowest hole concentration in low oxygen partial pressure. The results confirm that the Mn doping in small quantity could change drastically the defect configuration for the BCZT ceramics, which would have a great influence on the electrical properties.

3.4 Electrical properties

Figure 7(a) shows the P – E hysteresis loops measured at 1 Hz for the BCZT

ceramics sintered under different atmospheres. The maximum polarization (P_{\max}), remnant polarization (P_r), and coercive electric field (E_c) are summarized in Table 3. Figure 7(b)–(c) shows the bipolar and unipolar S – E curves measured at 1 Hz for BCZT ceramics. The bipolar S – E curves for all samples show a typical “butterfly” shape and the symmetrical structure, indicating the low defect concentration in the ceramics. The electrical properties such as piezoelectrical constant (d_{33}), electro–mechanical coupling factor (k_p), dielectric constant (ε_{33}^T), dielectric loss ($\tan\delta$), and the dynamic piezoelectric coefficient ($d_{33}^* = \frac{S_{\max}}{E_{\max}}$, also known as converse piezoelectric coefficient) at 40 kV/cm are summarized in Table 4. 0Mn–O ceramics samples possess the higher $P_{\max} = 18.9 \mu\text{C}/\text{cm}^2$ and $P_r = 10.45 \mu\text{C}/\text{cm}^2$ compared with 0Mn–N and 0Mn–A ceramics. At room temperature, the dynamic piezoelectric constant of 0Mn–O ceramics is 412 pm/V and the unipolar stress–strain reaches 0.17% at 40 kV/cm, indicating the excellent piezoelectric response of 0Mn–O ceramics. Furthermore, 0Mn–O achieves the highest $d_{33} = 585 \text{ pC}/\text{N}$, $k_p = 56\%$, and $\varepsilon_{33}^T = 4621$, which are better than 0Mn–A and 0Mn–N. Additionally, the $\tan\delta$ and E_c decrease when the undoped ceramics are sintered in O_2 , indicating that 0Mn–O ceramics have the lowest defect content. Therefore, the undoped ceramics exhibit the highest insulation resistivity and piezoelectric properties.

In the Mn-doped ceramics, 0.25Mn–N ceramics samples possess the higher $P_{\max} = 18.5 \mu\text{C}/\text{cm}^2$, $P_r = 9.38 \mu\text{C}/\text{cm}^2$, $d_{33} = 505 \text{ pC}/\text{N}$, $k_p = 50\%$, $\varepsilon_{33}^T = 4261$ and lower $E_c = 2.16 \text{ kV}/\text{cm}$ compared with 0.25Mn–O and 0.25Mn–A ceramics. Its dynamic piezoelectric constant and unipolar stress–strain reach up to 345 pm/V and 0.13% at

40 kV/cm, respectively. The Mn-doped ceramics sintered in N₂ have the lowest hole concentration in reference to the Hall and impedance analysis. The small number of point defects could facilitate the domain flipping and then enhance the electrical properties.

4. Conclusion

The relationship between defect configuration, electrical properties, and sintering atmosphere for the BCZT ceramics was systematically investigated and theoretically analyzed. The doping Mn element in BCZT ceramics can modulate the intrinsic conduction mechanism and then control the optimal sintering atmospheres. Based on impedance spectroscopy and Hall effect, the undoped ceramics exhibit an n-type conduction mechanism, and the electron concentration for the ceramics sintered under high oxygen partial pressure is minimized. Therefore, the undoped ceramics sintered in O₂ has the highest piezoelectric properties ($d_{33} = 585$ pC/N, $k_p = 56\%$). The Mn-doped ceramics exhibit a p-type conduction mechanism, and the hole concentration reduce with the decreasing oxygen partial pressure. The experimental results demonstrate that 0.25 mol% Mn-doped ceramics sintered in N₂ has the highest piezoelectric properties ($d_{33} = 505$ pC/N, $k_p = 50\%$). This work demonstrates that defect engineering could modulate the intrinsic conduction mechanism and electrical properties. It provides an effective way to predict the optimal sintering atmosphere for the BCZT ceramics.

Supporting Information

Supporting Information is available from the author.

Declaration of Competing Interest

The authors declare that they have no known competing financial interests or personal relationships that could have appeared to influence the work reported in this paper.

Acknowledgements

The work was supported by the National Natural Science Foundation of China (Grant Nos. 52072150, 51972146), Young Elite Scientists Sponsorship Program by CAST, State Key Laboratory of New Ceramic and Fine Processing Tsinghua University (No. KF202002) and Open Foundation of Guangdong Provincial Key Laboratory of Electronic Functional Materials and Devices (EFMD2021002Z).

References:

- [1] Tressler J, Alkoy S, Newnham R. Piezoelectric sensors and sensor materials. *J Electroceram* 1998, **2**: 257–272.
- [2] Hao J, Li W, Zhai J, *et al.* Progress in high-strain perovskite piezoelectric ceramics. *Mater Sci Eng R Rep* 2019, **135**: 1–57.
- [3] Gao X, Wu J, Yu Y, *et al.* Giant piezoelectric coefficients in relaxor piezoelectric ceramic PNN–PZT for vibration energy harvesting. *Adv Funct Mater* 2018, **28**: 1706895.
- [4] Jamie R, Graeme EB, Pedro JJA. Nanomaterials in the environment: Behavior, fate, bioavailability, and effects—An updated review. *Environ Toxicol Chem* 2018, **37**: 2029–2063.
- [5] Gao JH, Xu DZ, Liu F, *et al.* Recent progress on BaTiO₃-based piezoelectric ceramics for actuator applications. *Actuators* 2017, **6**: 24.
- [6] S Mahmoud A, C K, James Raju. Structural, dielectric, electromechanical, piezoelectric, elastic and ferroelectric properties of lanthanum and sodium co-substituted barium titanate ceramics. *J Alloys Compd* 2018, **737**: 464–476.
- [7] Li T, Lou X, Ke X, *et al.* Giant strain with low hysteresis in A-site-deficient (Bi_{0.5}Na_{0.5})TiO₃-based lead-free piezoceramics. *Acta Mater* 2017, **128**: 337–344.
- [8] Yin J, Zhao C, Zhang Y, *et al.* Ultrahigh strain in site engineering-independent Bi_{0.5}Na_{0.5}TiO₃-based relaxor-ferroelectrics. *Acta Mater* 2018, **147**: 70–77.
- [9] Wang K, Yao FZ, Koruza J, *et al.* Electromechanical properties of CaZrO₃ modified (K,Na)NbO₃-based lead-free piezoceramics under uniaxial stress conditions. *J Am Ceram Soc* 2017, **100**: 2116–2122.
- [10] Li P, Chen XQ, Wang FF, *et al.* Microscopic insight into electric fatigue resistance and thermally stable piezoelectric properties of (K,Na)NbO₃-based ceramics. *ACS Appl Mater Interfaces* 2018, **10**: 28772–28779.
- [11] Barbara M, Jurij K, Jitka H, *et al.* Sintering of lead-free piezoelectric sodium potassium niobate ceramics. *Mater* 2015, **8**: 8117–8146.
- [12] Castkova K, Maca K, Cihlar J, *et al.* Chemical synthesis, sintering and

- piezoelectric properties of $\text{Ba}_{0.85}\text{Ca}_{0.15}\text{Zr}_{0.1}\text{Ti}_{0.9}\text{O}_3$ lead-free ceramics. *J Am Ceram Soc* 2015, **98**: 2373–2380.
- [13] Li SB, Wang CB, Li L, *et al.* Effect of annealing temperature on structural and electrical properties of BCZT ceramics prepared by Plasma Activated Sintering. *J Alloys Compd* 2018, **730**: 182–190.
- [14] Coondoo I, Panwar N, Alikin D, *et al.* A comparative study of structural and electrical properties in lead-free BCZT ceramics: influence of the synthesis method. *Acta Mater* 2018, **155**: 331–342.
- [15] Liu Y, Chang Y, Li F, *et al.* Exceptionally high piezoelectric coefficient and low strain hysteresis in grain-oriented $(\text{Ba,Ca})(\text{Ti,Zr})\text{O}_3$ through integrating crystallographic texture and domain engineering. *ACS Appl Mater Interfaces* 2017, **9**: 29863–29871.
- [16] Bai WF, Chen DQ, Peng L, *et al.* Enhanced electromechanical properties in textured $(\text{Ba}_{0.85}\text{Ca}_{0.15})(\text{Zr}_{0.1}\text{Ti}_{0.9})\text{O}_3$ lead-free piezoceramics. *Ceram Int* 2016, **42**: 3429–3436.
- [17] Liu W, Ren X. Large piezoelectric effect in Pb-free ceramics. *Phys Rev Lett* 2009, **103**: 257602.
- [18] Gao RL, Chu XC, Huan Y, *et al.* Ceramic–electrode inter-diffusion of (K, Na) NbO_3 -based multilayer ceramics with $\text{Ag}_{0.7}\text{Pd}_{0.3}$ electrode. *J Eur Ceram Soc* 2015, **35**: 389–392.
- [19] Zhang QW, Cai W, Zhou C, *et al.* Electric fatigue of BCZT ceramics sintered in different atmospheres. *Appl Phys A* 2019, **125**: 759.
- [20] Cai W, Zhang QW, Zhou C, *et al.* Effects of oxygen partial pressure on the electrical properties and phase transitions in $(\text{Ba,Ca})(\text{Ti,Zr})\text{O}_3$ ceramics. *J Mater Sci* 2020, **55**: 9972–9992.
- [21] Zhang SW, Zhang HL, Zhang BP, *et al.* Dielectric and piezoelectric properties of $(\text{Ba}_{0.95}\text{Ca}_{0.05})(\text{Ti}_{0.88}\text{Zr}_{0.12})\text{O}_3$ ceramics sintered in a protective atmosphere. *J Eur Ceram Soc* 2009, **29**: 3235–3242.
- [22] Yao ZH, Luo Q, Xu CB, *et al.* Titanium deficiency in tetragonal-structured

- (Ba,Ca)(Zr,Ti)O₃ piezoelectric ceramics. *J Alloys Compd* 2017, **712**: 406–411.
- [23] Wang H, Yuan H, Hu Q, *et al.* Exploring the high-performance (1-x)BaTiO₃-xCaZrO₃ piezoceramics with multiphase coexistence (R-O-T) from internal lattice distortion and domain features. *J Alloys Compd* 2021, **853**: 157167.
- [24] Dobal PS, Katiyar RS. Studies on ferroelectric perovskites and Bi-layered compounds using micro-Raman spectroscopy. *J Raman Spectrosc* 2002, **33**: 405–423.
- [25] Janbua W, Bongkarn T, Kolodiazhnyi T, *et al.* High piezoelectric response and polymorphic phase region in the lead-free piezoelectric BaTiO₃-CaTiO₃-BaSnO₃ ternary system. *RSC Adv* 2017, **7**: 30166–30176.
- [26] Perry CH, Hall DB. Temperature Dependence of the Raman Spectrum of BaTiO₃. *Phys Rev Lett* 1965, **15**: 700–702.
- [27] Zhang YM, Deng HM, Si SF, *et al.* Band gap narrowing and magnetic properties of transition-metal-doped Ba_{0.85}Ca_{0.15}Ti_{0.9}Zr_{0.1}O₃ lead-free ceramics. *J Am Ceram Soc* 2019, **103**: 2491–2498.
- [28] Zhang Y, Sun HJ, Chen W. Influence of cobalt and sintering temperature on structure and electrical properties of BaZr_{0.05}Ti_{0.95}O₃ ceramics. *Ceram Int* 2015, **41**: 8520–8532.
- [29] Chen XL, He F, Wang YL, *et al.* Significant effects of powder preparation processes on the physical properties of Bi_{0.5}Na_{0.5}TiO₃-0.06BaTiO₃ ceramic. *J Mater Sci Mater Electron* 2014, **25**: 5309–5315.
- [30] Bae SH, Kahya O, Sharma BK, *et al.* Graphene-P(VDF-TrFE) multilayer film for flexible applications. *Acs Nano* 2013, **7**: 3130–3138.
- [31] Wang ZX, Huan Y, Feng Y, *et al.* Design of p-type NKN-based piezoelectric ceramics sintered in low oxygen partial pressure by defect engineering. *J Am Ceram Soc* 2020, **103**: 3667–3675.
- [32] Li M, Pietrowski MJ, De Souza RA, *et al.* A family of oxide ion conductors based on the ferroelectric perovskite Na_{0.5}Bi_{0.5}TiO₃. *Nat Mater* 2014, **13**: 31–35.
- [33] Donnelly NJ, Randall CA. Mixed conduction and chemical diffusion in a

Pb(Zr_{0.53},Ti_{0.47})O₃ buried capacitor structure. *Appl Phys Lett* 2010, **96**: 1060.

Figure captions:

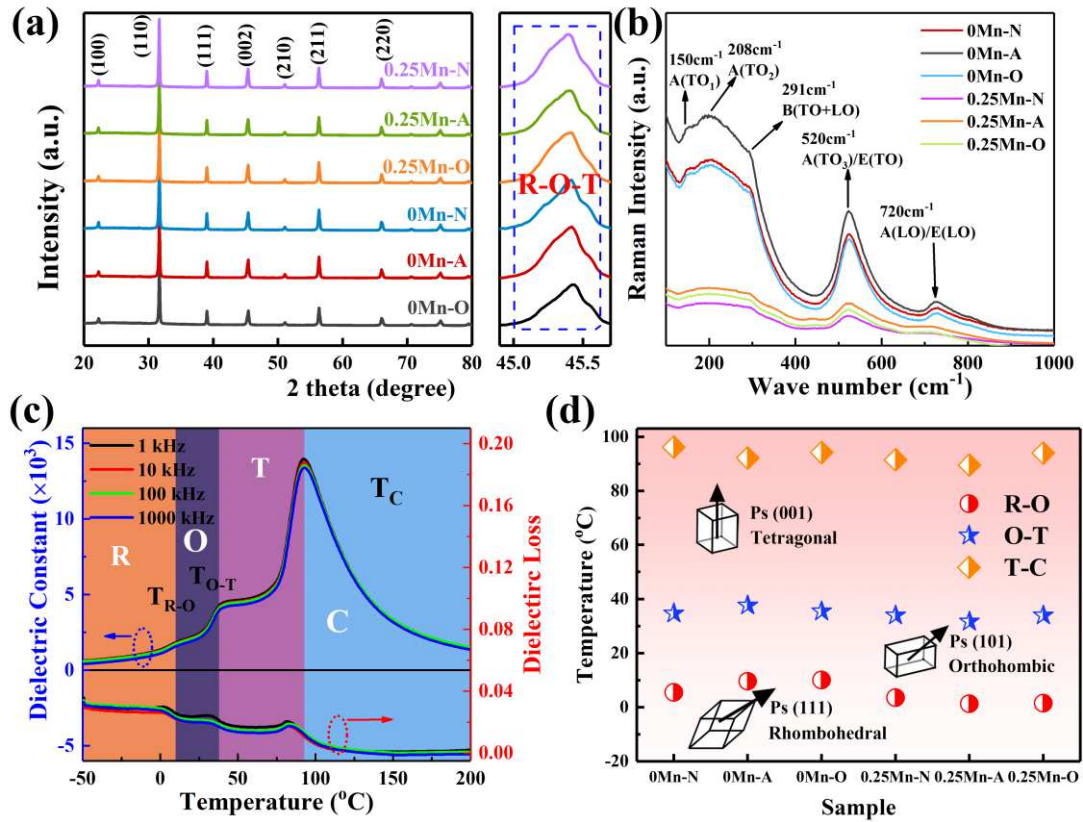


Figure 1 (a) XRD patterns of the BCZT ceramics in 2θ range of $20 - 80^\circ$ and $44.9 - 45.7^\circ$; (b) Room-temperature Raman spectra of the BCZT ceramics; (c) Dielectric constant and loss of 0Mn-A sample as a function of temperature; (d) The phase transition temperatures of the BCZT ceramics.

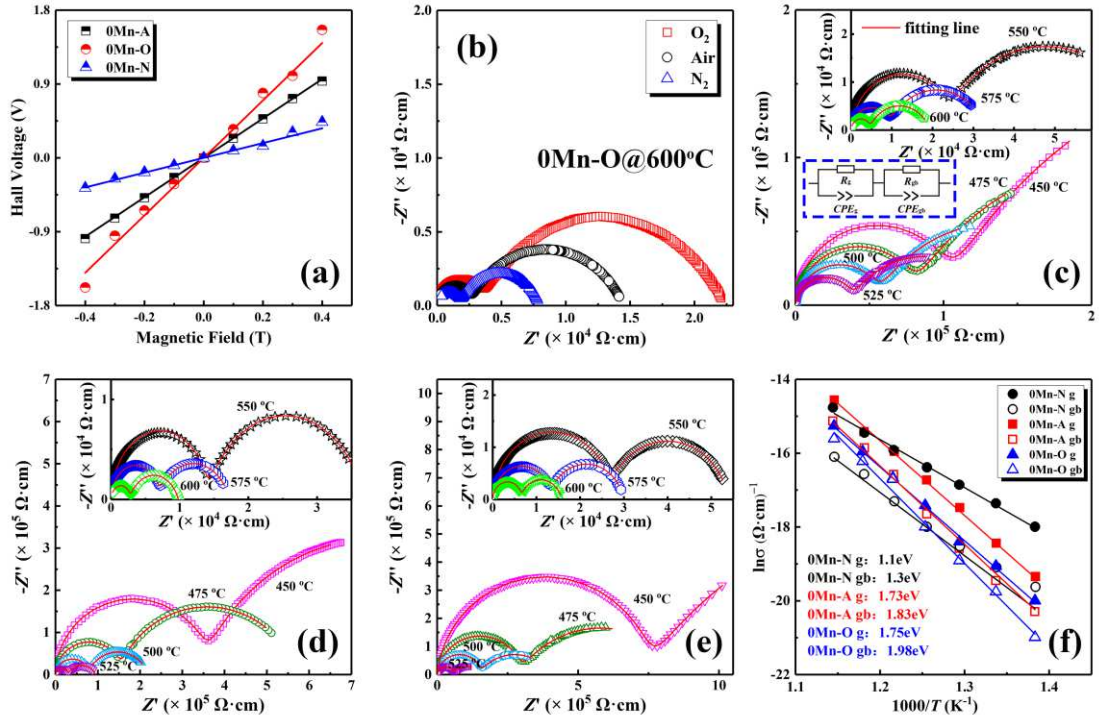


Figure 2 (a) Voltage as a function of applied magnetic field (0Mn–N, 0Mn–A, 0Mn–O); (b) Impedance spectrum of 0Mn–O measured at 600 °C in nitrogen, air and oxygen respectively; (c)–(e) Impedance spectra of the 0Mn–N, 0Mn–A and 0Mn–O measured at 450 °C–600 °C in air; (f) Arrhenius plots and the fitted E_a values of 0Mn–N, 0Mn–A, 0Mn–O.

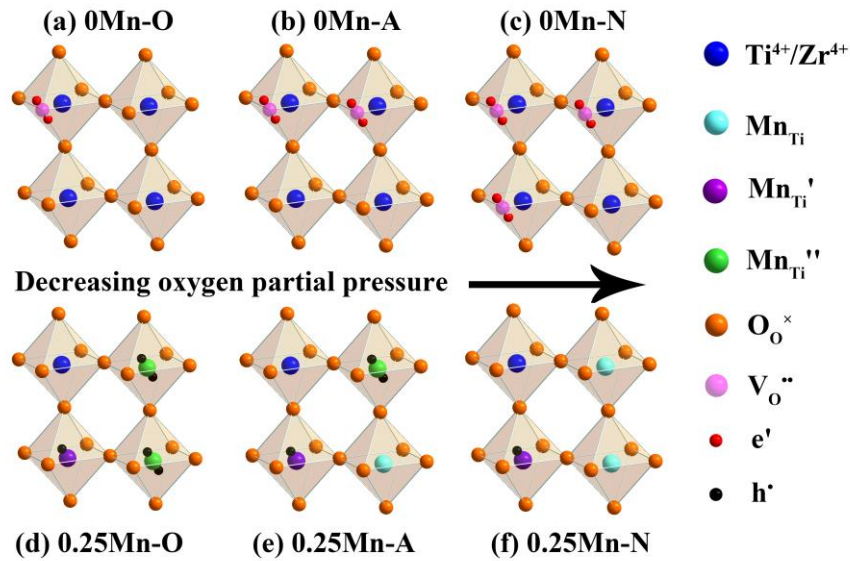


Figure 3 Schematic diagrams of defect configuration for BCZT based ceramics.

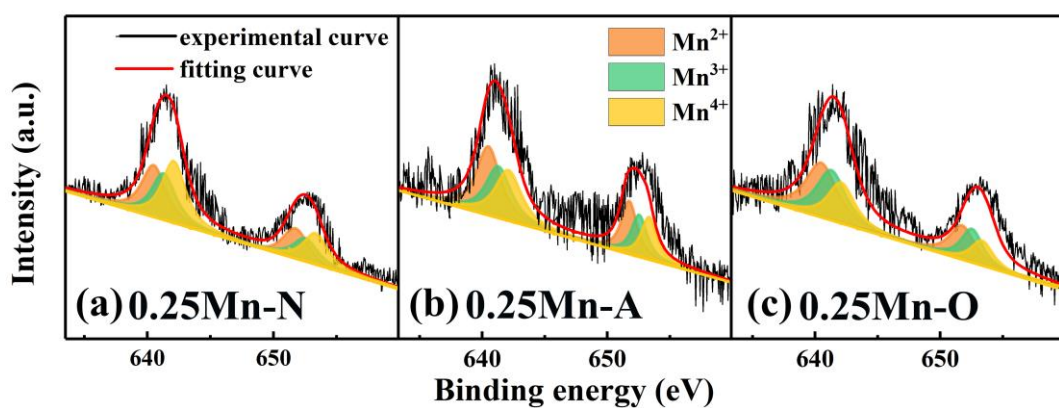


Figure 4 High-resolution Mn 2p spectra and the corresponding fitting curves of (a) 0.25Mn-N, (b) 0.25Mn-A, and (c) 0.25Mn-O.

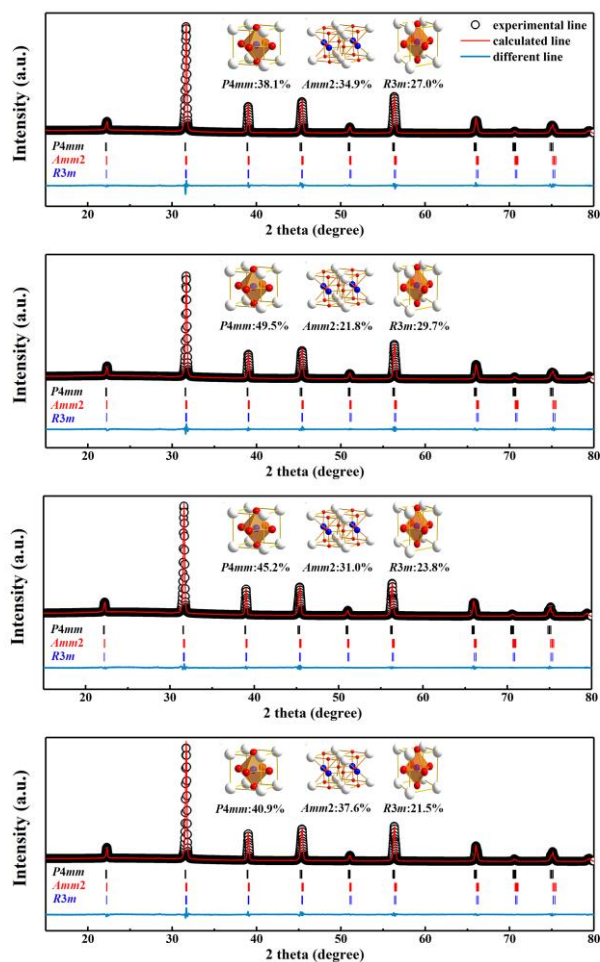


Figure 5 XRD patterns and Rietveld refinement results of BCZT ceramics: (a) 0Mn-A; (b) 0.25Mn-N; (c) 0.25Mn-A; (d) 0.25Mn-O.

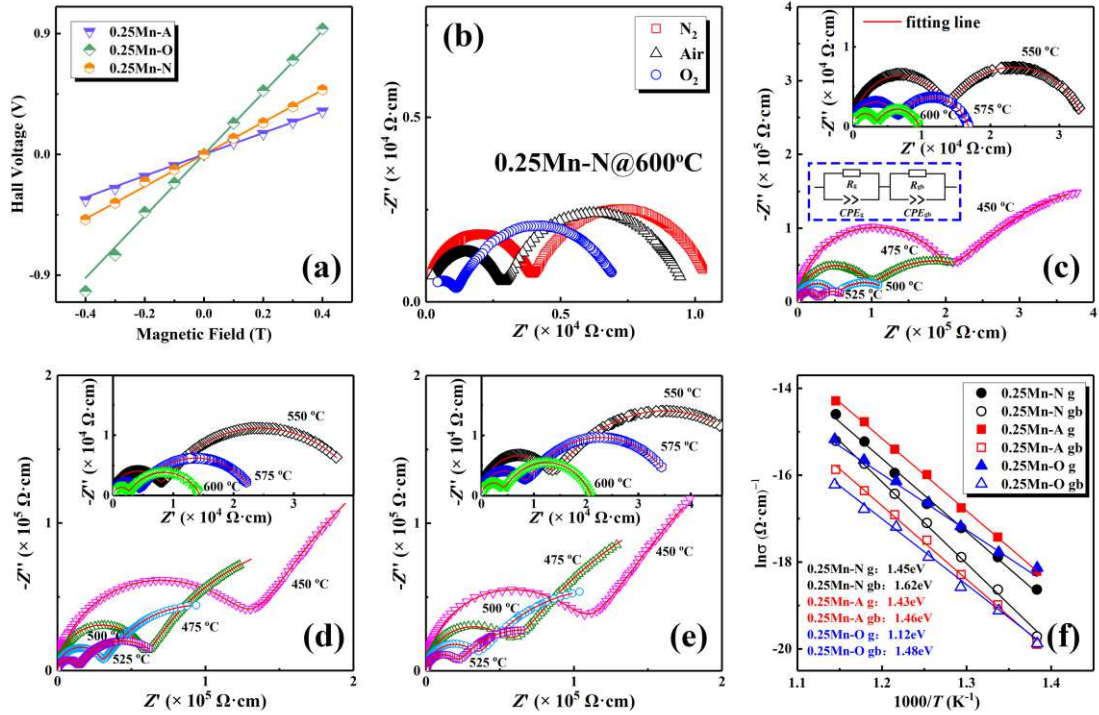


Figure 6 (a) Voltage as a function of applied magnetic field for 0.25Mn–N, 0.25Mn–A, and 0.25Mn–O samples; (b) Impedance spectrum of 0.25Mn–N measured at 600 °C in nitrogen, air and oxygen; Impedance spectra of the (c) 0.25Mn–N, (d) 0.25Mn–A and (e) 0.25Mn–O at 450 °C–600 °C in air; (f) Arrhenius plots and the fitted E_a values of 0.25Mn–N, 0.25Mn–A, 0.25Mn–O

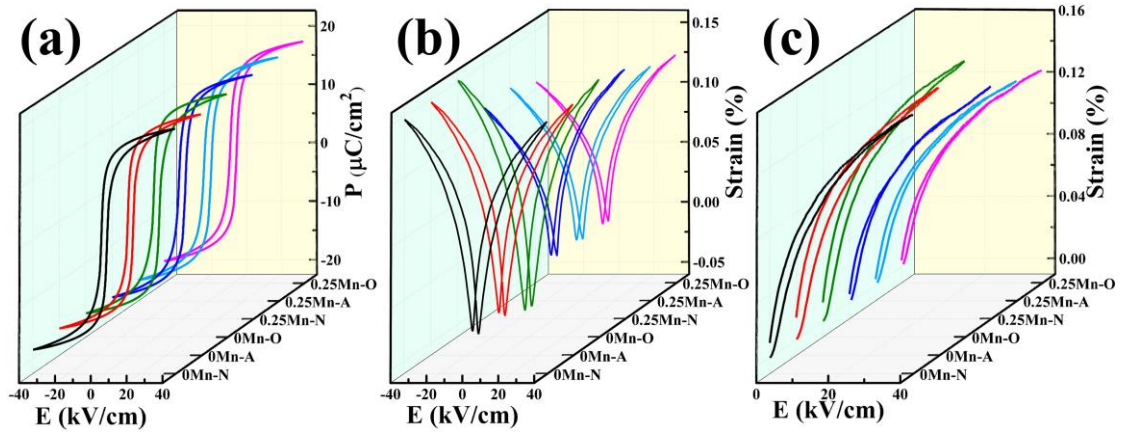


Figure 7 the P – E hysteresis loops (a), the bipolar S – E curves (b) and the unipolar S – E curves (c) measured at 1 Hz for BCZT ceramics sintered in different atmospheres.

Tables:

Table 1 Carrier type, carrier concentration, and Hall resistivity of the BCZT ceramics sintered in different atmospheres

sample	carrier type	concentration (cm ⁻³)	Hall resistivity (Ω·cm)
0Mn-N	n	4.22×10 ⁷	1.54×10 ⁷
0Mn-A	n	2.05×10 ⁷	2.40×10 ⁷
0Mn-O	n	1.28×10 ⁷	4.38×10 ⁷
0.25Mn-N	p	1.05×10 ⁸	1.28×10 ⁷
0.25Mn-A	p	2.28×10 ⁸	1.04×10 ⁷
0.25Mn-O	p	3.59×10 ⁸	5.50×10 ⁶

Table 2 Lattice parameters and refinement parameters of BCZT ceramics obtained from XRD Rietveld refinement

sample	Space group	a (Å)	b (Å)	c (Å)	α (°)	R _{wp} (%)
0Mn-A	P4mm	3.9951	3.9951	4.0063	90	7.60
	Amm2	3.9916	5.6558	5.6527	90	
	R3m	3.9981	3.9981	3.9981	90.0059	
0.25Mn-N	P4mm	3.9799	3.9799	4.0070	90	6.81
	Amm2	3.9908	5.6598	5.6561	90	
	R3m	4.0084	4.0084	4.0084	89.7982	
0.25Mn-A	P4mm	3.9919	3.9919	3.9980	90	5.99
	Amm2	3.9919	5.6620	5.6763	90	
	R3m	3.9977	3.9977	3.9977	90.1750	
0.25Mn-O	P4mm	3.9909	3.9909	3.9990	90	6.09
	Amm2	3.9993	5.6664	5.6730	90	
	R3m	4.0043	4.0043	4.0043	89.8550	

Table 3 The maximus polarization (P_{\max}), the remnant polarization (P_r), and the coercive electric field (E_c) obtained from the P-E hysteresis loops

	P_{\max} (μC/cm ²)	P_r (μC/cm ²)	E_c (kV/cm)
0Mn-N	18.7	9.7	1.81

0Mn-A	18.8	10.2	1.46
0Mn-O	18.9	10.45	1.23
0.25Mn-N	18.5	9.38	2.16
0.25Mn-A	18.45	9.29	2.26
0.25Mn-O	18	9.02	2.15

Table 4 Electrical properties of the BCZT ceramics sintered in different atmospheres

sample	d_{33} (pC/N)	k_p (%)	$\tan\delta$	ϵ_{33}^T	d_{33}^* (pm/V)
0Mn-N	483	49	0.018	4054	382
0Mn-A	540	52	0.018	4338	397
0Mn-O	585	56	0.014	4621	412
0.25Mn-N	505	50	0.013	4261	345
0.25Mn-A	458	45	0.014	3893	325
0.25Mn-O	432	43	0.015	3880	315

Figures

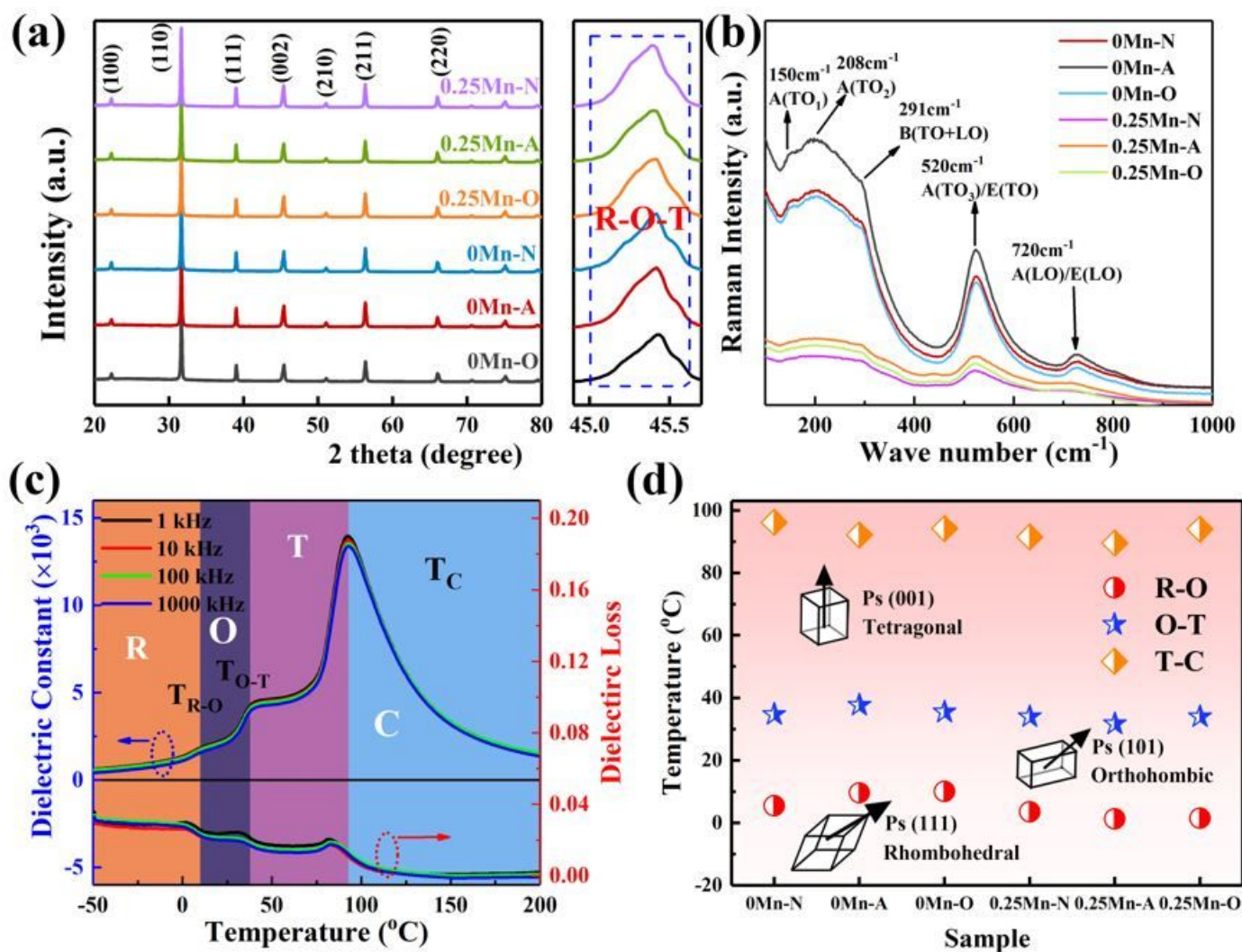


Figure 1

please see the manuscript file for the full caption

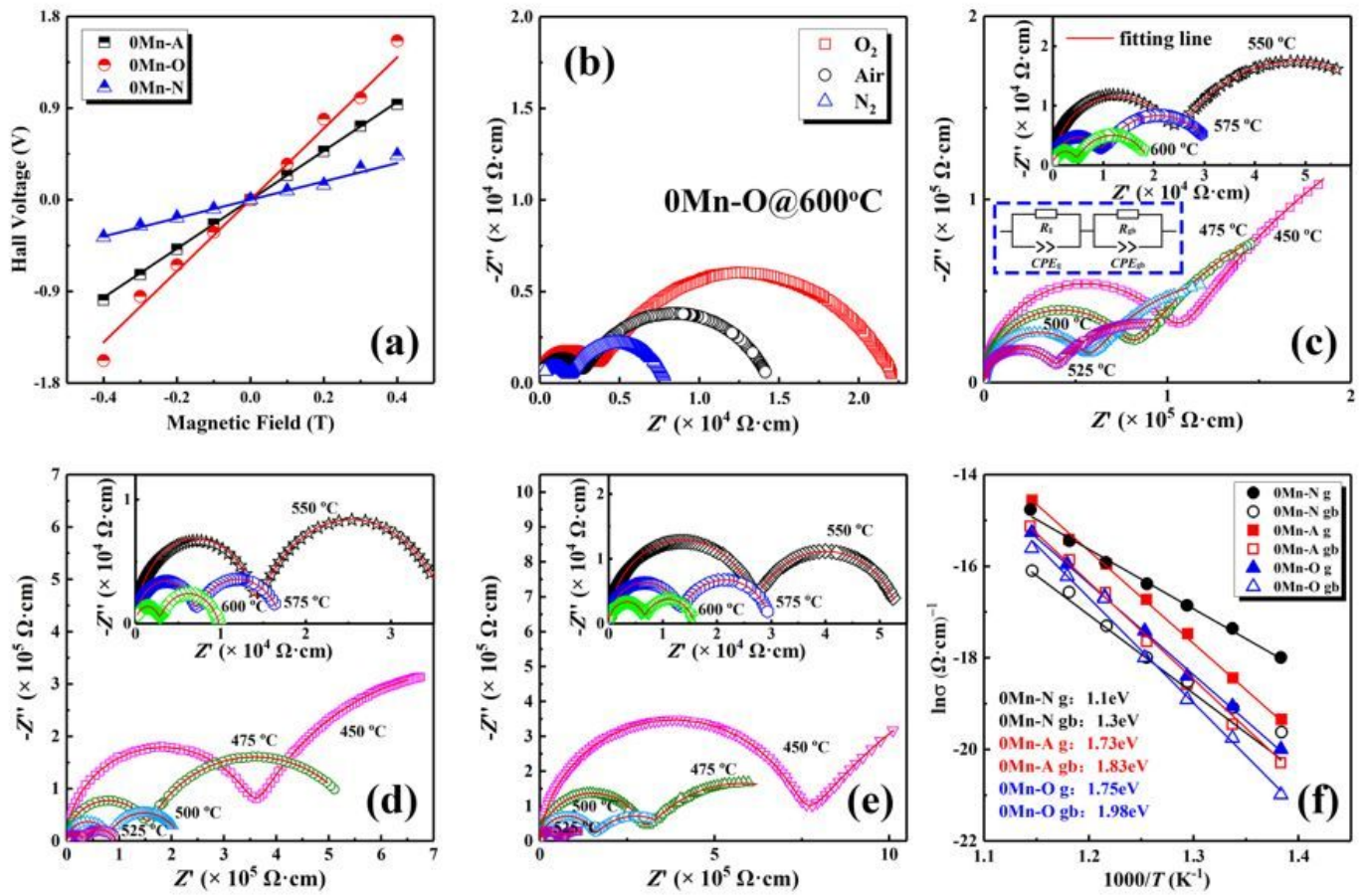


Figure 2

please see the manuscript file for the full caption

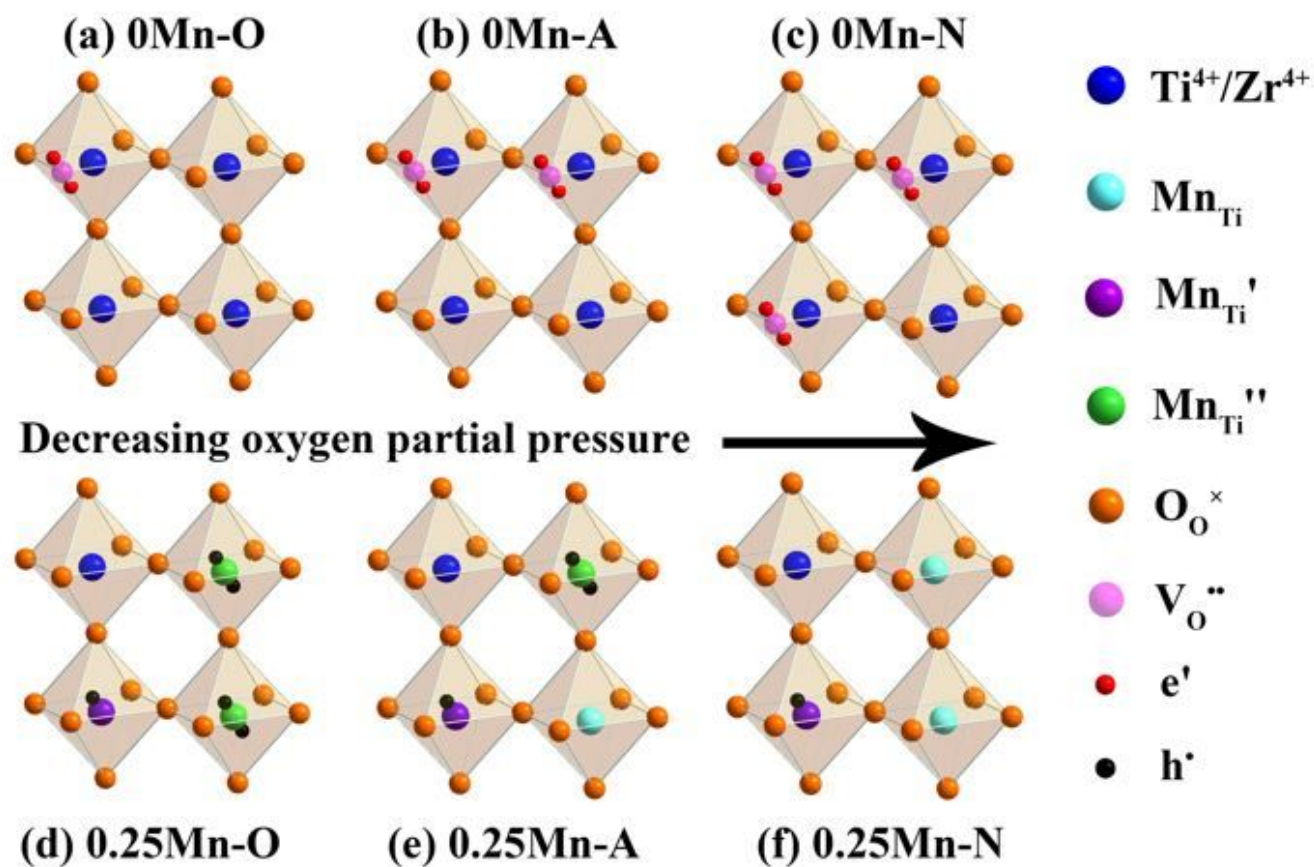


Figure 3

Schematic diagrams of defect configuration for BCZT based ceramics.

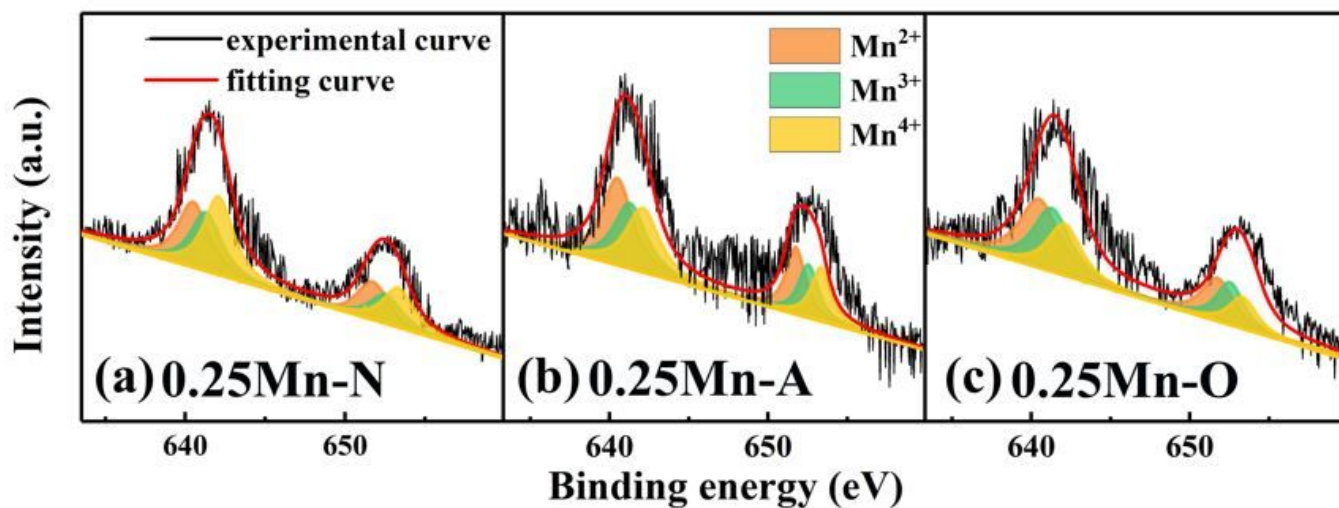


Figure 4

High-resolution Mn 2p spectra and the corresponding fitting curves of (a) 0.25Mn-N, (b) 0.25Mn-A, and (c) 0.25Mn-O.

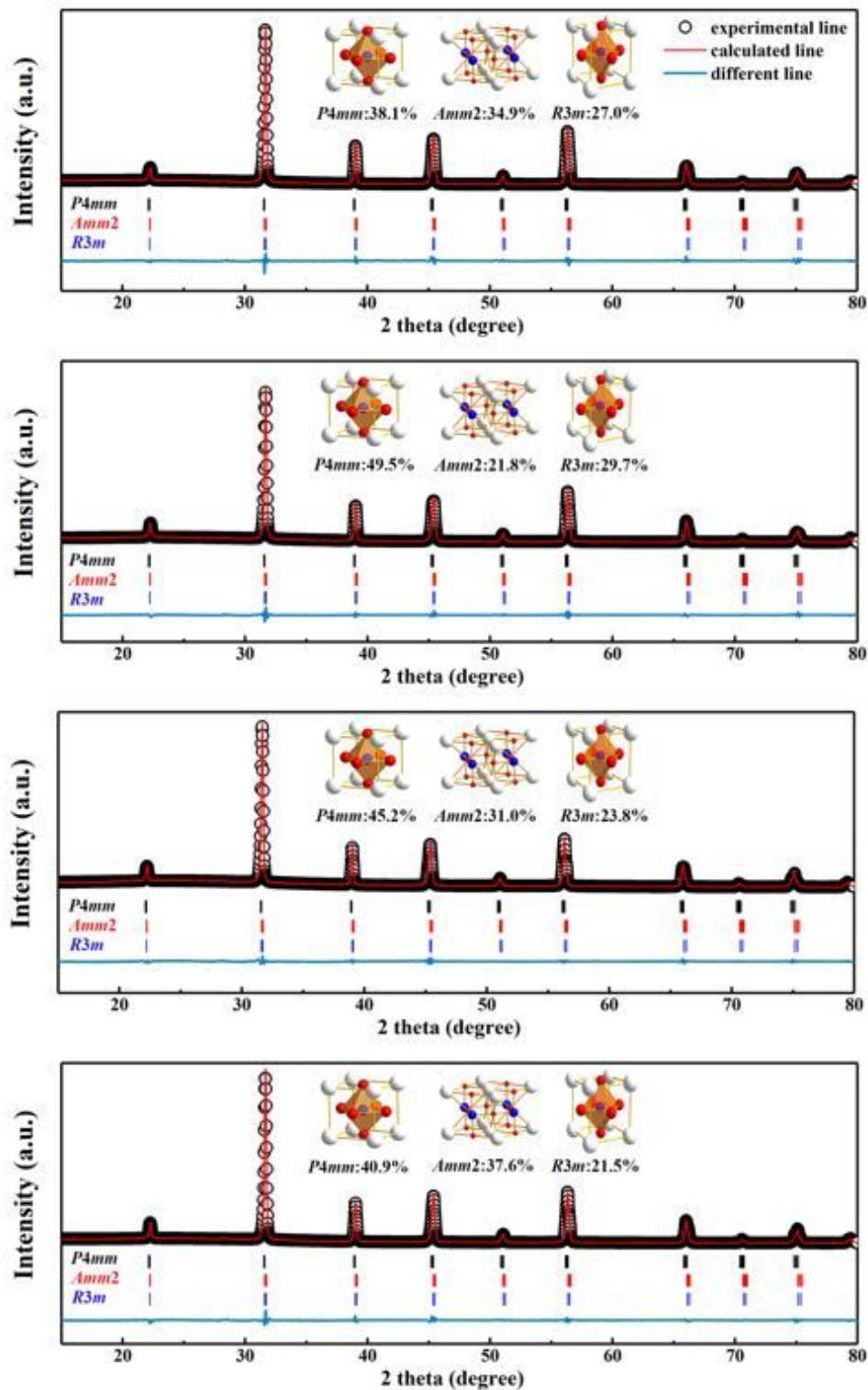


Figure 5

XRD patterns and Rietveld refinement results of BCZT ceramics: (a) 0Mn-A; (b) 0.25Mn-N; (c) 0.25Mn-A; (d) 0.25Mn-O.

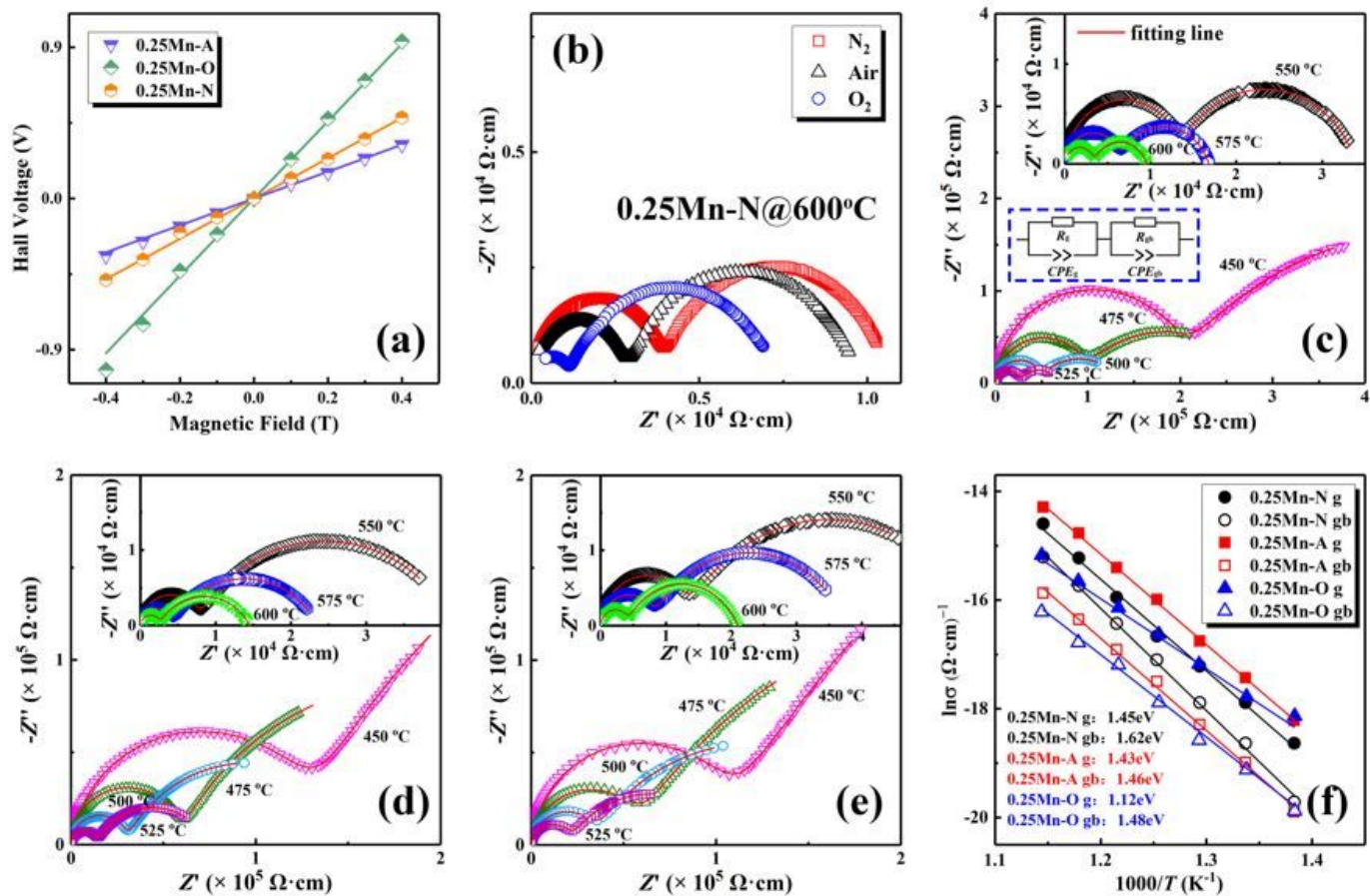


Figure 6

(a) Voltage as a function of applied magnetic field for 0.25Mn-N, 0.25Mn-A, and 0.25Mn-O samples; (b) Impedance spectrum of 0.25Mn-N measured at 600 oC in nitrogen, air and oxygen; Impedance spectra of the (c) 0.25Mn-N, (d) 0.25Mn-A and (e) 0.25Mn-O at 450 oC–600 oC in air; (f) Arrhenius plots and the fitted E_a values of 0.25Mn-N, 0.25Mn-A, 0.25Mn-O

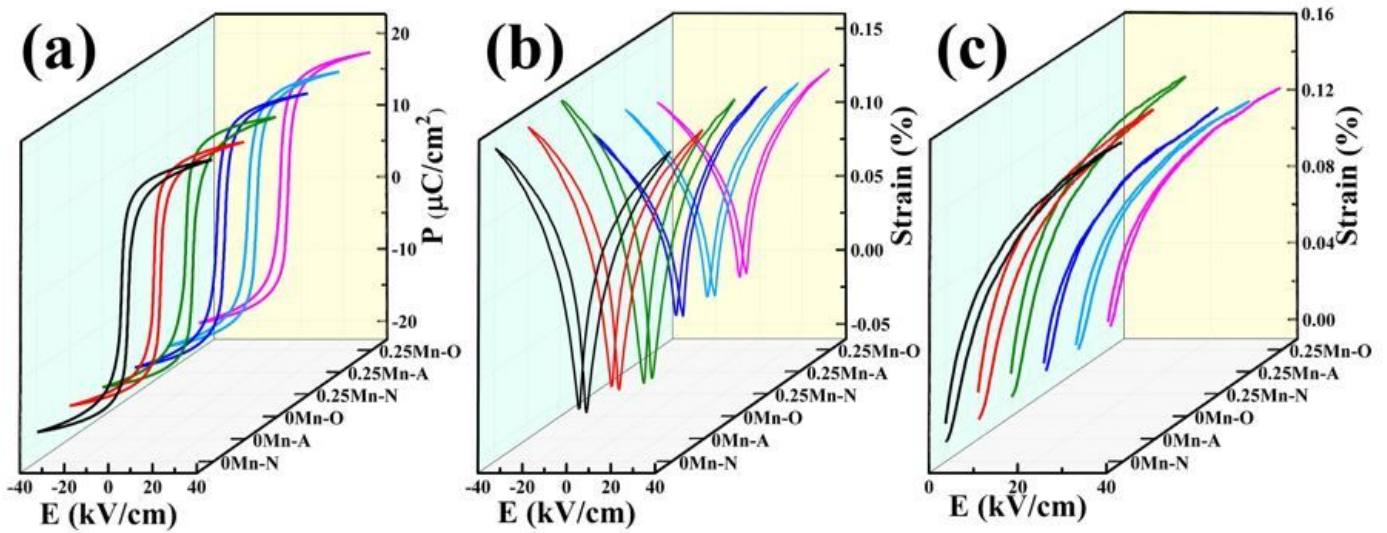


Figure 7

the P–E hysteresis loops (a), the bipolar S–E curves (b) and the unipolar S–E curves (c) measured at 1 Hz for BCZT ceramics sintered in different atmospheres.

Supplementary Files

This is a list of supplementary files associated with this preprint. Click to download.

- [supportinginformation.docx](#)